

Article

# Tribological Properties and Corrosion Resistance of Porous Structure Ni-Mo/ZrO<sub>2</sub> Alloys

Ning Li \*, Hong Xu, Xinhui Li, Weizeng Chen, Lijuan Zheng and Lirong Lu

Xingzhi College, Zhejiang Normal University, Jinhua 321004, China; Xuh@zjnu.cn (H.X.); huilai1212@126.com (X.L.); jdxcwz@zjnu.cn (W.C.); zhenglj@zjnu.cn (L.Z.); llr@zjnu.cn (L.L.)

\* Correspondence: ln2316@zjnu.edu.cn or lintlt515@126.com; Tel.: +86-0579-822-91191

Received: 25 June 2020; Accepted: 4 August 2020; Published: 7 August 2020



**Abstract:** Ni-Mo-ZrO<sub>2</sub> composite coatings were produced by pulse electrodeposition technique from alkaline electrolytes containing dispersed ZrO<sub>2</sub> nanopowder. The structure, microhardness, corrosion properties and tribological properties of Ni-Mo-ZrO<sub>2</sub> composites with different content of molybdenum and ZrO<sub>2</sub> have also been examined. Structural characterization was performed using X-ray diffraction (XRD) and a scanning electron microscope (SEM). It was found that an increase in molybdate concentration in the electrolyte affects the microstructure, microhardness, corrosion properties and tribological properties of the amount of co-deposited ZrO<sub>2</sub> nanoparticles. The incorporation of ZrO<sub>2</sub> nanoparticles into the Ni-Mo alloy matrix positively affects the microhardness and also slightly improves the corrosion properties of Ni-Mo alloy coatings. In addition, both the coefficient of friction and the salt-water lubrication sliding wear rate of Ni-Mo-ZrO<sub>2</sub> coatings decreased with increasing the ZrO<sub>2</sub> content. Wear test and corrosion resistance test results indicated that the intermetallic composite had an excellent wear-resistance and corrosion resistance at room-temperature, which is attributed to the high hardness and strong atomic bonding of constituent phases Ni-Mo and polarization effect of ZrO<sub>2</sub> nanoparticles.

**Keywords:** Ni-Mo-ZrO<sub>2</sub> alloys; corrosion resistance; tribological properties; microstructure

## 1. Introduction

Nano-sized zirconia (ZrO<sub>2</sub>) is an important structural and functional material. It is the only transition metal oxide with acidity and alkalinity as well as oxidizing and reducing properties. It has high chemical stability and thermal stability and is widely used on the composite coating. The Ni-based composite coating doped with ZrO<sub>2</sub> nanoparticles has high hardness, wear resistance and high temperature resistance, and has been used in various parts, such as the inner wall of a gas turbine, the engine of a jet aircraft, the ship transportation, and the electronics industry. In the literature [1–4], the influence of the preparation process of the Ni-ZrO<sub>2</sub> composite coating on the morphology of the coating and the corrosion performance in different media was analyzed and discussed. The study shows that the Ni-ZrO<sub>2</sub> composite coating has extremely high corrosion resistance. Studies with respect to tribological properties of Ni-Mo coatings are rarely documented [5,6]. Huang et al. [5] indicated that the wear resistance of pulsed electrodeposited coatings improved, compared to DC electrodeposited Ni-Mo alloy. Lehman et al. [6] illustrated that the wear rate and friction coefficient for Ni-Mo coatings deposited at higher current density (low Mo content) was lower than that of those deposited at lower current density (high Mo content) from a citrate electrolyte [7–11]. All these studies attribute improved wear resistance to the hardness and surface roughness of the coatings in a qualitative manner. In addition, the comparative performance evaluation of Ni-Mo and HCr coatings is also not documented in open literature. Wasekar et al. [7] studied the properties and structure of Ni-W/SiC composite coatings strengthened by nano-SiC. It was pointed out that, although the nano-SiC

was peeled off during the heat treatment of the composite coating, it still had good corrosion resistance. Due to the small particle size and high surface energy of the nanoparticles, the agglomeration is highly likely to occur in the plating solution, and finally the particles in the plating layer are present in an agglomerated state, thereby degrading the performance of the nanocomposite coating. When the concentration of the nanoparticles is relatively low, they are dispersed in the monodisperse state in the composite coating. Since the nanoparticles are not only small in size, their Orowan strengthening effect is extremely remarkable, and the hardness of the composite coating is improved.  $ZrO_2$  is positively charged, and the addition of a cationic surfactant increases the charge of the particulate  $ZrO_2$  and migrates faster toward the cathode, which is advantageous for increasing the amount of the composite. In order to improve the material's activity and service life, the applications of  $ZrO_2$  composites in the field of catalysis are very extensive [12–16]. However, there are few studies on the preparation of reinforcement materials as porous materials, especially in the field of energy electrodes, and composite materials of this type are being designed for using in nuclear, energy, and fuel cells fields, etc. [15,16]. Ni-Mo- $ZrO_2$  composite coating was prepared by the pulse electrodeposition method. The structure, corrosion resistance, and wear resistance of the Ni-Mo- $ZrO_2$  composite coating were studied in order to obtain Ni-Mo- $ZrO_2$  composite coating with high corrosion resistance and wear resistance.

## 2. Materials and Methods

### 2.1. Composite Plating Process

During the experiment, the interference of other impurity elements was minimized, and the plating solution was prepared by using double distilled water, and the chemicals were all analytically pure. The composition of the base plating solution is as follows:  $48\text{ g}\cdot\text{L}^{-1}$  of  $NiCO_3\cdot 2Ni(OH)_2\cdot 4H_2O$  (calculated as Ni,  $\geq 44.0\%$ , Sinopharm Chemical Reagent Co., Ltd., Shanghai, China),  $10\text{ g}\cdot\text{L}^{-1}$   $(NH_4)_2MoO_4\cdot 2H_2O$  ( $\geq 99.0\%$ , Hefei University of Technology Reagent Factory, Hefei, China),  $60\text{ g}\cdot\text{L}^{-1}$  ammonium citrate ( $(NH_4)_3C_6H_5O_7\cdot H_2O$ ) ( $\geq 99.0\%$ ),  $20\text{ g}\cdot\text{L}^{-1}$  sodium chloride ( $\geq 99.0\%$ ),  $18\text{ g}\cdot\text{L}^{-1}$  of  $H_3BO_3$  ( $\geq 99.5\%$ ),  $2.4\text{ g}\cdot\text{L}^{-1}$  of saccharin ( $\geq 99.0\%$ ),  $24\text{ mL}\cdot\text{L}^{-1}$  of self-adapting additive ( $0.3\text{ g}\cdot\text{L}^{-1}$  of twelve Sodium alkyl sulfate ( $C_{12}H_{25}NaO_4S$ ) and  $1.0\text{ g}\cdot\text{L}^{-1}$  of oxalic acid ( $C_2H_2O_4$ )). The pH value is controlled during the plating process,  $pH = 9.0 \pm 0.1$ , adjusted with a 5% ammonium citrate solution, and temperature  $40 \pm 2\text{ }^\circ\text{C}$ . In the composite plating experiment, the modified nano  $ZrO_2$  particles have a particle size of  $20\text{--}30\text{ nm}$  (The  $ZrO_2$  particle size is provided by the supplier) and  $4\text{ g}\cdot\text{L}^{-1}$ .

The anode was made of foamed nickel plate ( $W_{Ni} = 99.96\%$ ), the cathode was made of low carbon steel (working area:  $7\text{ mm} \times 7\text{ mm} \times 40\text{ mm}$ ), the area ratio of cathode to anode was 1:4, the pitch between the two poles was 20 mm, and the non-working surface was insulated with epoxy resin. Before electrodeposition, the cathode working surface was treated to remove the oxide film on the surface, and then de-oiled and activated with acetone and 10% dilute hydrochloric acid solution, and then rinsed with distilled water for use. A DF-101S constant temperature water bath and collector-type magnetic heating stirrer (Henan Gongyi Yingyu Yuhua Instrument, Zhengzhou, China) was used to control bath temperature and stirring speed ( $200\text{ r}\cdot\text{min}^{-1}$ ). The power supply uses a pulse power supply SMD-P series intelligent multi-pulse plating power supply (Hebei Handan Dawei Electroplating Equipment Co., Ltd., Handan, China) at a duty ratio 1:14 and current density of  $1.0\text{ A}\cdot\text{cm}^{-2}$ .

### 2.2. Structure and Morphology Analysis

The grain size can also be calculated by transmission electron microscopy (TEM, Japan Eletron Optics Laboratory Co., LTD., Tokyo, Japan) or scanning electron microscopy (SEM, Hitachi S-4800, 15 kV, Hitachi, Tokyo, Japan) using diagonal measurement method. When the grain size is less than 100 nm, the stress-induced broadening can be neglected compared with the grain size-induced broadening. At this point, Scherrer's formula is relatively adaptable. The coating structure analysis was carried out on a Philips X'pert MPD Pro X-ray diffractometer (XRD, Bruker SMART APEX II,

BrukerSmart, Rheinstetten, Germany) with a tube voltage of 35 kV, a Cu target, and a scan speed of  $4^\circ \cdot \text{min}^{-1}$ . The average grain size is calculated using the Scherrer formula [4–7] by measuring the position of the X-ray diffraction peak ( $\theta$  angle), the material crystal orientation equation  $2d \sin\theta = \lambda$ , and the Equation (1) [17–20].

$$d = \frac{a}{\sqrt{\frac{4}{3}(h^2 + k^2hk) + \left(\frac{a}{c}\right)^2 l^2}} \quad (1)$$

where  $(h, k, l)$  is the crystal plane index,  $\lambda$  is the incident X-ray wavelength, and  $a$  and  $c$  are the  $a$ -axis and  $c$ -axis constants of the crystal. The magnitude of the microscopic stress can be calculated by the equation  $\bar{\sigma} = \frac{E\beta_D}{4\tan\theta}$ . Where  $\bar{\sigma}$  is the average stress,  $E$  is the Young's modulus,  $\beta_D$  is the full width at half maximum, and  $\theta$  is the peak position of the diffraction peak.

### 2.3. Corrosion Resistance Test

In the static soaking experiment, the prepared  $7 \text{ mm} \times 7 \text{ mm}$  sheet sample was immersed in a 4% NaCl (analytical pure) solution, soaked for 24 h, and the mass change and surface morphology of the sample were measured to determine the corrosion resistance. The degree of corrosion of the plating layer can be evaluated by the corrosion rate. From the perspective of economy and practicability, the temperature of the corrosive medium was set to room temperature ( $25^\circ \text{C}$ ), and the corrosion loss after the corrosion of each sample was measured to obtain the respective corrosion. At the same time, in order to ensure the accuracy and reliability of the experimental data, each set of test pieces in the experiment was three pieces, and the corrosion rate was taken as the average value. The corrosion rate is defined as the mass change caused by the corrosion of a corroded sample per unit area per unit time. Its expression is:  $v = \Delta G/s \times t$  ( $\text{mg}/\text{cm}^2 \cdot \text{h}$ ). Samples before and after corrosion must be subjected to four steps of rinsing with deionized water, ultrasonic cleaning with ethanol, drying, and weighing. The balance used for the experimental weighing was an AE240 electronic analytical balance, and the surface morphology of the corroded sample was observed by scanning electron microscopy.

### 2.4. Friction and Wear Test

The friction and wear properties of the composites were tested on an MMW-1A vertical universal friction and wear tester (Jinan Yihua Tribology Testing Technology Co., Ltd., Jinan, China). The designed cross-section of the sample was  $7 \times 7 \text{ mm}^2$  and the length was 40 mm. The contact surface of the sample was coated with a certain thickness of Ni-ZrO<sub>2</sub> or Ni-Mo-ZrO<sub>2</sub> composite coating. The material of the grinding ring block was GCr15 steel with a hardness of 56HRC, and the test pin and the test ring were polished with 800# water sandpaper and washed with acetone before the experiment. During the experiment, the ring was stationary and the square pin rotated. The wear amount of the pin is expressed by the specific wear rate, which is defined as the wear quality per unit load multiplied by the sliding distance. The calculation expression is as follows:

$$\omega_s = \frac{\Delta m}{sp} \quad (2)$$

where:  $\omega_s$  is the specific wear rate—the unit is  $\text{kg}/(\text{N m})$ ;  $\Delta m$  is the wear quality loss of the sample (kg);  $s$  is the sliding distance (m);  $p$  is the normal load of the friction pin (N).

At room temperature and normal pressure—intravenous saline (0.9% NaCl), 65–70 drops/min, experimental load 20 kg, sample rotation speed 200 r/min, wear time 60 min, total stroke 3168 m—the average value of the friction coefficient of 30 min after the state is stabilized was taken as the stable friction factor, and the average value of the three experimental results was taken. The wear quality was determined by weighing the test piece before and after the test using the AE240 electronic analytical balance (accuracy of 0.1 mg). The surface morphology was characterized by a S-4800 high-resolution field emission scanning electron microscope (Hitachi S-4800, 15 kV). The Vickers hardness tester used in this test was modeled as MVC-1000B with a load of 500 g·F and a loading time of 15 s.

### 3. Experimental Results and Analysis

#### 3.1. Coating Composition and Morphology

The composition analysis results of the electrodeposition coating are shown in Figure 1. Different from the growth crystal orientation of the conventional nickel alloy [2], the Ni-Mo coated layer (Figure 1a) and the Ni-ZrO<sub>2</sub> composite coated layer (Figure 1b) obtained in this experiment preferentially grow with the (200) crystal plane [17,20], which may be in the alkali under the environmental conditions of the deposition solution—excessive additive ions are adsorbed on the surface of the metal crystal, which changes the normal growth direction of Ni (111) [20–23]. At the same time, the literature [3,4] pointed out that the embedding of ZrO<sub>2</sub> nanoparticles will greatly weaken the growth of Ni ions on the (220) crystal plane, enhance the 2θ to the diffraction peak near 52°, and then show the preferential growth of crystal on the (200) crystal plane orientation. Figure 1c shows the XRD pattern of the Ni-Mo-ZrO<sub>2</sub> composite coating. It can be seen that, in addition to the diffraction peak of ZrO<sub>2</sub>, there is a corresponding diffraction peak of the Ni-Mo alloy. The addition of nanoparticles makes the diffraction peak of the composite coating on the growth plane wide, and the Ni-Mo alloy and ZrO<sub>2</sub>, respectively, exhibit their diffraction characteristic peaks at specific angles without mutual interference. This is due to the addition of nanoparticles, which reduce the overpotential of the metal nucleation reaction, and act as a new nucleation growth point, which plays a role in refining the grains. The dispersion strengthening effect of ZrO<sub>2</sub> nanoparticles is remarkable. A broadening diffraction peak appears near 2θ ≈ 44°, but the peak shape is not smooth enough, and a little sharp peak is included, indicating that the coating is not completely determined as crystalline or amorphous [24]. This change is due to the large difference in crystal structure and lattice constant of ZrO<sub>2</sub> and Ni. In order to keep the lower system energy, it is necessary to form a composite coating with a certain interface between Ni and ZrO<sub>2</sub> particles. Ni is a crystal with a face-centered cubic structure, and the (111) crystal plane is the lowest energy crystal plane. Therefore, this matching interface relationship promotes the growth of the Ni (111) crystal plane during the growth process. The average grain sizes of Ni-ZrO<sub>2</sub> and Ni-Mo-ZrO<sub>2</sub> composite coatings were calculated by the Scherrer Equation to be about 14.3 and 16.7 nm—the corresponding conditions are shown in Table 1, respectively. According to the analysis, as of the embedding of nano-ZrO<sub>2</sub> particles, the growth of the original crystal is hindered, which affects the crystal orientation of grain growth. Another reason may be the pulse perturbation effect on changing the deposition mode of the nickel matrix and causing the growth pattern of the substrate change.

Figure 2 shows the surface morphology of four electrodeposited coatings. It can be seen from Figure 2 that the structure of the pulse deposition coating is small, the surface is even and flat, the particles take on the shape of sand particles or cauliflower-like structure characteristics, the visualization particles are fine (the observed deposited particle size is about 1 μm, and there are smaller particles in the larger particles), the grain boundary becomes blurred, the spatial structure is present, and the cluster structure is relatively dense. The particles of the alloy coating containing Mo element are smaller, the gap between the particles increase, and the compactness of the overall surface of the coating becomes dispersed. The grain compactness of the alloy coating containing ZrO<sub>2</sub> is more obvious. The nano-ZrO<sub>2</sub> particles added to the deposition solution are positively charged due to the adsorption of H<sup>+</sup> and Ni<sup>2+</sup> in the deposition solution, and the increase in the thickness of the pulse diffusion layer causes a large concentration polarization. A large amount of hydrogen gas is adsorbed on the surface of the cathode, which leads to nickel and the pH of the interface between the deposition solutions rising sharply, increasing the adsorption and eutectoids of some insoluble materials on the cathode surface. The reduction of the Ni ions at the substrate interface encapsulates the adsorbed nano-ZrO<sub>2</sub> particles in the electrodeposited layer, so as to form a composite plating layer containing the nanoparticles. On the other hand, under the action of fluid dynamics and current, the ion concentration difference increases and the surface effect and size effect of the nanoparticles are conducive to the formation of new crystal nuclei, which increases the growth point of the deposited crystal grains to some extent and improves electroplating. The nucleation rate and the adsorption and deposition of the dispersed and insoluble

matter at the crystal growth point will inhibit the growth of the crystal, so as to obtain a fine crystal structure [25,26].

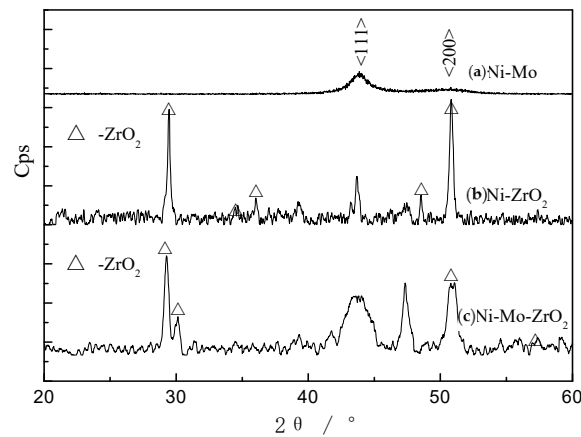


Figure 1. XRD patterns of deposited.

Table 1. Effect of nano-ZrO<sub>2</sub> particle content on microhardness of composite Ni-Mo coatings.

ZrO <sub>2</sub> in Solution (g/L)	Mass Fraction of ZrO <sub>2</sub> (%)	Microhardness (HV)	Average Crystalline Size (nm)	Wear Mass Loss (mg)	Steady Friction Coefficient	Corrosion Rate (mg/cm <sup>2</sup> h)
4 (No Molybdate)	3.68	614	14.3	8.5	0.102	0.066
0	0	535	18.3	15.6	0.30	0.052
2	1.24	596	17.1	6.2	0.21	0.064
4	3.96	653	16.7	3.5	0.136	0.04
8	6.54	694	14.2	2.6	0.124	0.035
16	8.17	662	18.5	4.3	0.142	0.072
20	8.12	621	20.2	10.1	0.33	0.108

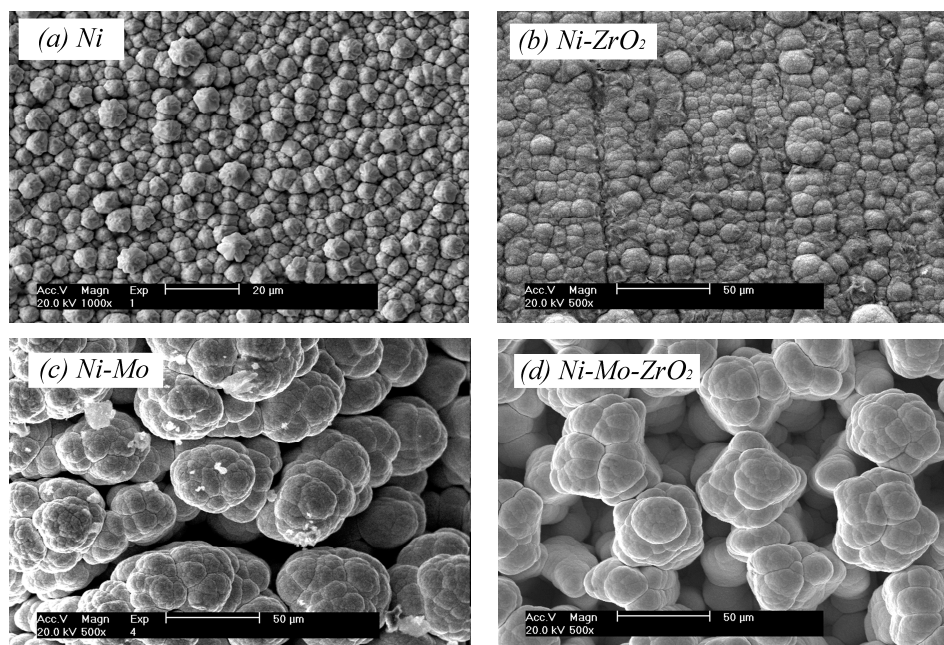


Figure 2. SEM images of the deposited coatings.

It can also be seen from Figure 2 that the morphology of the composite coating of Ni-ZrO<sub>2</sub> (Figure 2b) and Ni-Mo-ZrO<sub>2</sub> (Figure 2d) exhibits a three-dimensional structure with overlapping layers between layers. This may be related to the pulse current efficiency, and, at the same time, the edge of the deposited layer has a higher discharge potential at the time of deposition, thereby facilitating

adsorption of the chelate group, realizing the ion reduction process. Comparing the two composite coatings, it is found that the Ni-Mo-ZrO<sub>2</sub> composite coating exhibits a more regular spatial structure, and the agglomerated particles deposited are more uniform and finer, which may be related to the presence of molybdate chelate in the deposition bath, and molybdenum ions. The reduction process is multi-step reduction, the energy to be absorbed is large, and the reduction will delay the deposition process of nickel ions, and the dispersion distribution of nano-ZrO<sub>2</sub> particles further delays the mutual coupling of nickel ions and nickel–molybdenum ions, resulting in the deposition and further refining of the ions. The surface morphology is layered and deepened as space structure with a regular pentagon or hexagonal structure, which is related to the nuclear power of the ZrO<sub>2</sub> particles. The nuclear power stability of each particle forms a certain electric field distribution, and the particles within the relative dimensional stability range will interact and stabilize and finally be arranged to form an orderly spatial structure.

### 3.2. Hardness of Composite Coating

The hardness values of the composite coatings are shown in Table 1, and the morphologies of the Ni-Mo alloy containing ZrO<sub>2</sub> nanoparticles are shown in Figure 3. It can be seen from Table 1 that in the nickel-molybdenum deposition solution, the introduction of ZrO<sub>2</sub> nanoparticles significantly increases the microhardness of the as-deposited and refines the grain size. At the same time, the hardness of the Ni-Mo alloy coating is greatly improved by the nanoparticles. The hardness value is increased from HV535 to the highest value of HV694, and the average grain size is first decreased and then increased. When the addition amount of the nanoparticles is continuously increased, the hardness of the composite coating decreases slightly and the average grain size also increases. This is because the ZrO<sub>2</sub> particle—tetragonal and monoclinic with the dual properties of weak acid and weak base and the lower surface energy [27]—when the content of nanoparticles with a size of 11–30 nm is too high, a large number of particles easily produces agglomerate. Oxygen vacancies can interact with active substances uniquely. A large number of nanoparticles easily absorbs active groups, resulting in an intense impact between the added particles, reducing the recombination of particles, decreasing the cohesive force of the matrix and the hardness of the coating.

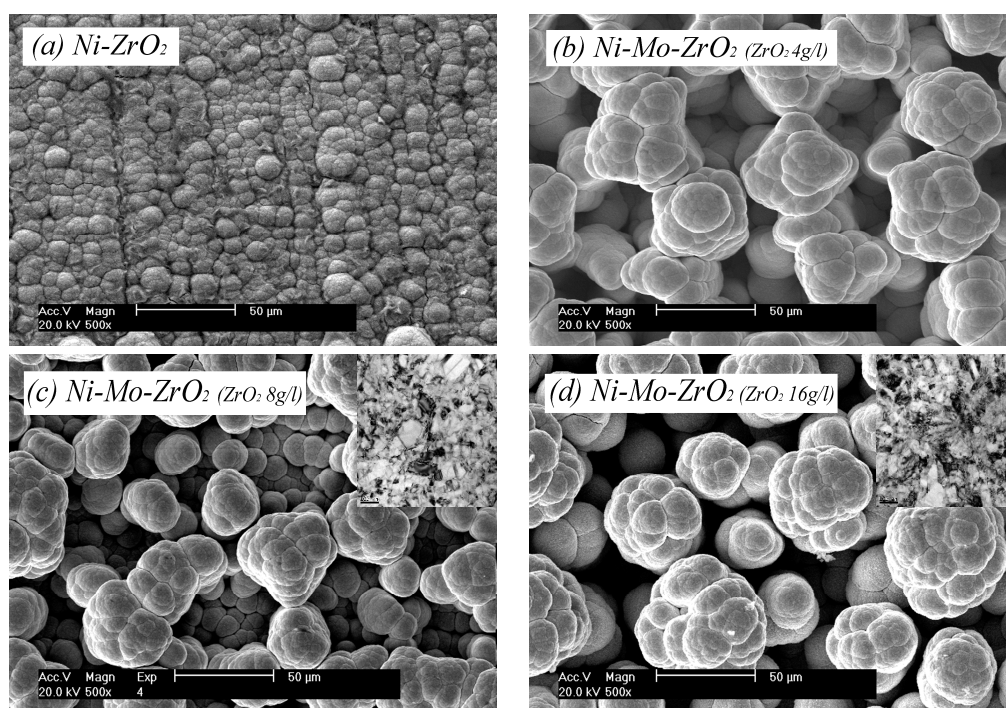


Figure 3. SEM and TEM images of the deposited composite Ni-Mo-ZrO<sub>2</sub> coatings.

The surface morphologies of Ni-Mo composite coatings with different ZrO<sub>2</sub> nanoparticles content are shown in Figure 3. It can be seen from the morphologies that the introduction of nanoparticles will increase the surface roughness of the coating, and its morphology will show three-dimensional morphology. With the increase in ZrO<sub>2</sub> nanoparticles, the morphology of the deposited particles firstly has a regular structure and becomes disordered. This is related to the charge and charge of the ions adsorbed on the surface of the ZrO<sub>2</sub> nanoparticles. The carrying of a certain number of charges makes the particle-based group have a stable interdependence, resulting in a stable regular ordered structure during deposition. When the content of ZrO<sub>2</sub> nanoparticles exceeds a certain ratio, the nuclear balance is broken, and the deposited particles are returned to disorder. At the same time, it can be found that the gullies and mutual spacing between certain deposited particles will help to increase the actual surface of the coating, and the material of the structure has obvious activity advantages as a catalytic material and an electrode material [2–4]. The material is modified on the surface of the workpiece, and the change from surface contact to multi-point contact during the contact process will also effectively reduce the friction factor of the material and reduce the amount of wear. Under the condition of lubricating medium, the porous structure of this kind of structural material will also store more lubricant, which can further reduce the friction coefficient of the material and improve the service life.

### 3.3. Tribological Properties of Composite Coating

Under the condition of brine medium, combined with the friction coefficient and wear amount of the composite coatings with different contents of ZrO<sub>2</sub> nanoparticles in Table 1, the friction coefficient of a certain amount of nano-ZrO<sub>2</sub> composite coating is relatively low, and the friction coefficient is between 0.1–0.2. The wear amount is also low. When the content exceeds a certain value, the friction coefficient rises sharply and the friction coefficient of the Ni-Mo alloy plating layer containing no nanoparticles is almost equivalent, which is related to the agglomeration of the nanoparticles. The reason that the friction coefficient of the composite coating is relatively low is that the porous structure on the surface of the coating layer stores a certain amount of water. During the frictional contact, a water film is formed, which reduces the contact surface between the coating layer and the abrasive member, and the nanoparticle is hard. The dispersion enhancement enhances the hardness of the coating. This point–contact process further reduces the contact surface of the coating, which is characterized by a low coefficient of friction during friction and wear. The corrosion of brine is relatively large, especially under the dynamic conditions of the workpiece, and the instantaneous transfer effect of the contact surface will increase the possibility of corrosion of the material, but the experimental results show that the wear of the composite coating is also low in a short time, which is related to the fact that the matrix Ni-Mo alloy is related to abrasion resistance, and the literature [28,29] shows that the Ni-Mo alloy has extremely high corrosion resistance. At the same time, the ZrO<sub>2</sub> nanoparticles refine the grains, which also reduce the defect content in the coating and improve the compactness and corrosion resistance of the coating.

The surface morphologies of the composite coatings after wear are shown in Figure 4. According to the friction coefficient and wear amount of the coating of Table 1, the surface of the Ni-Mo coating without ZrO<sub>2</sub> nanoparticles has obvious corrosion marks, but there are not many corrosion pits, and the corrosion traces may be generated during the dynamic wear process. In the middle, the boundary between different crystal phases can be produced. There is no obvious corrosion mark in the Ni-ZrO<sub>2</sub> and Ni-Mo-ZrO<sub>2</sub> composite coatings containing ZrO<sub>2</sub> nanoparticles. During the friction and wear process, the composite coating is in contact with the surface of the abrasive. Under the action of salt water, the contact matrix metal slides and has potential change to change—the diffused high-hardness ZrO<sub>2</sub> particles play a supporting role in the interaction of the friction pair, which reduces the direct contact area between the matrix alloy with lower hardness and the pair of grinding pairs, and reduces the friction coefficient of the composite coating. The reduction in the contact area is also the main optimization factor for the reduction in wear. ZrO<sub>2</sub> nanoparticles completely buried in the surface

of the substrate are also subjected to contact force transmission, which alleviates the adhesive wear process of the coating. The agglomeration effect of the particles can be seen from Figure 4a, the  $ZrO_2$  nanoparticles can suppress the ploughing action of the micro-convex on the surface of the friction surface, weaken the micro-cutting of the coating, reduce the wear of the substrate, and greatly reduce the wear amount.

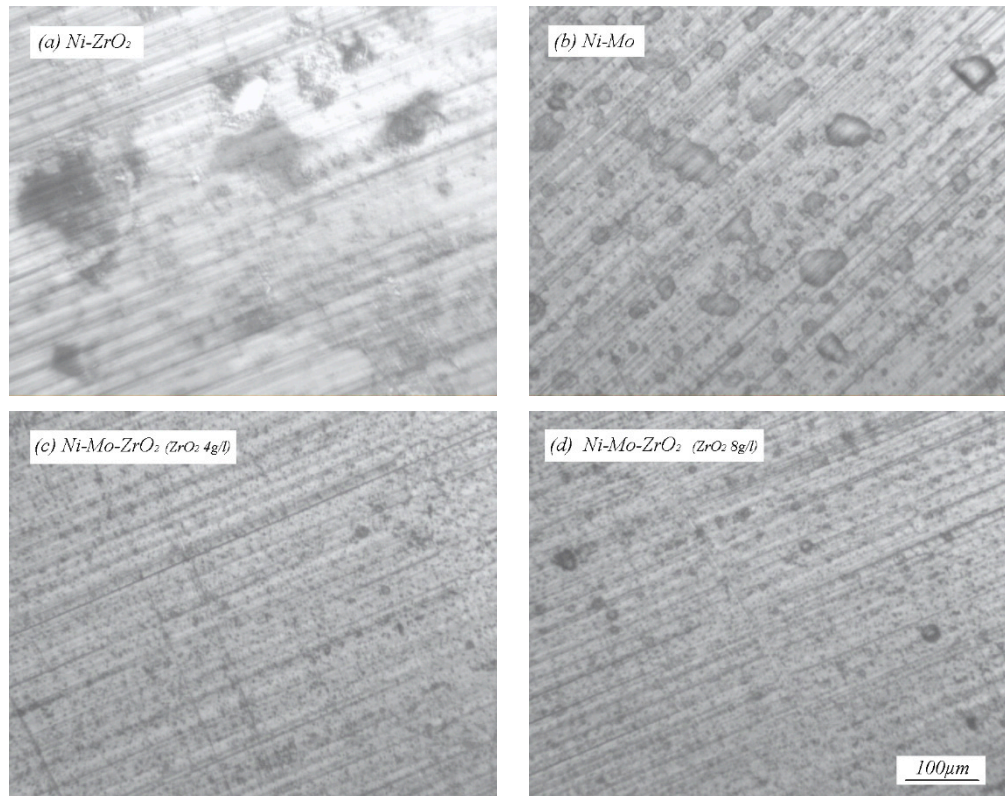


**Figure 4.** Metallographic surface morphologies of the coatings after wear.

### 3.4. Corrosion Resistance of Composite Coatings

The amount of coating loss after immersion corrosion for 24 h is shown in Table 1. The surface morphology of the etched coating is shown in Figure 5. It can be seen from the morphology that the surface of the coated nickel, nickel-molybdenum alloy and Ni-Mo- $ZrO_2$  has no obvious corrosion marks from the macroscopic surface, while the surface of Ni- $ZrO_2$  has a boundary corrosion effect, which is related to the agglomeration effect of the  $ZrO_2$  nanoparticles in the coating. The Ni and Ni-Mo coatings have obvious corrosion traces from the SEM morphologies surface. The grain boundary of Ni coating is corroded, and the Ni-Mo coating surface has more corrosion pits. A small amount of boundary corrosion marks can still be seen in the Ni- $ZrO_2$  coating. The Ni-Mo- $ZrO_2$  coating has almost no corrosion traces. Because the  $ZrO_2$  nanoparticles have a bipolar effect, the charge capacity adsorbed on the surface of the particles makes them balance in the suspension and deposit into the interior of the coating during the deposition process, and the agglomeration effect will increase between the particle phase and the matrix phase. The potential difference means that the boundary has obvious corrosion marks, while in the other three layers, the potential difference between the reinforcing phase and the matrix phase is relatively balanced, and as with the Ni-Mo alloy coating, the  $ZrO_2$  nanoparticles will further enhance the composite coating corrosion resistance. With the introduction of  $ZrO_2$  particles, a composite oxide layer is easily formed on the surface of the coating. The composite oxide layer plays the role of passive film in the corrosion process because of its continuity and integrity. At the same time, grain refinement can also have the effect of fine grain strengthening, which can further improve

the corrosion resistance of the coating. It can be seen that the Ni-Mo-ZrO<sub>2</sub> composite coating has better corrosion resistance by the frictional corrosion performance of the coating under salt-water conditions.

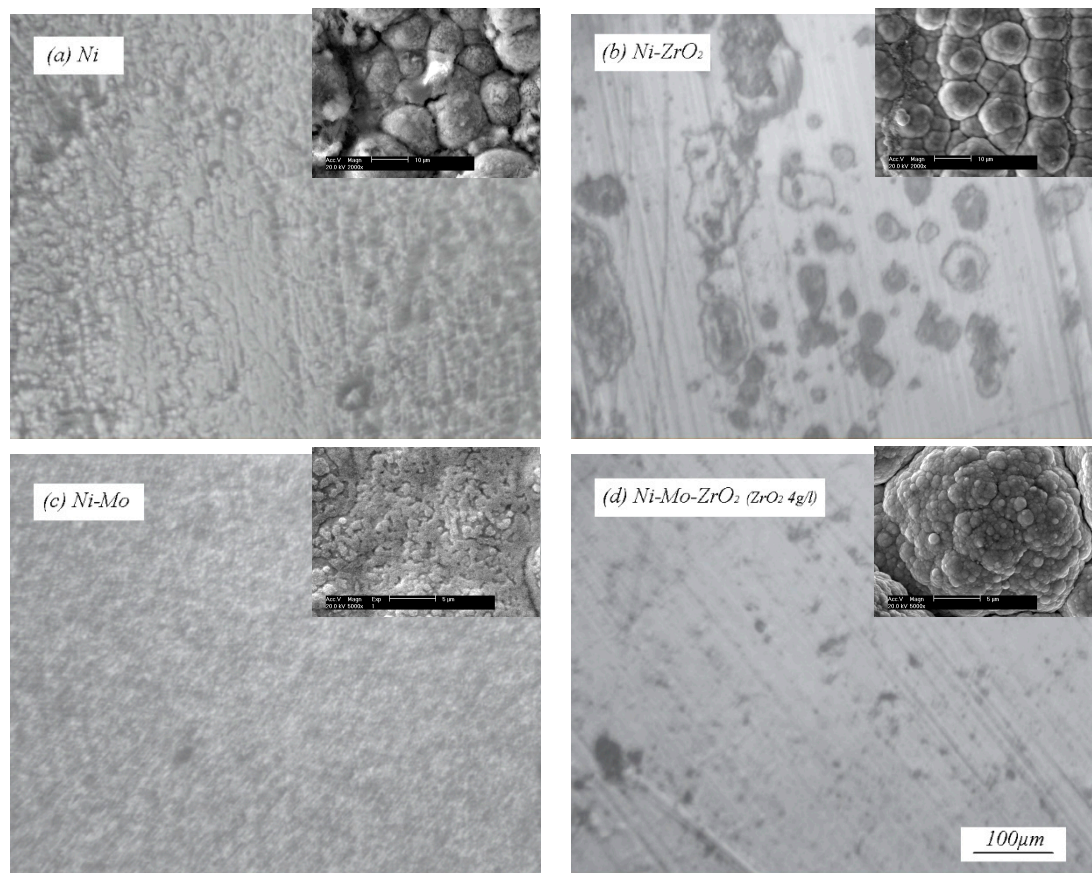


**Figure 5.** Metallographic surface morphologies and SEM images of the coatings after corrosion resistance.

#### 4. Conclusions

- The nano-ZrO<sub>2</sub> particles with polarity affect the surface morphology of the coating and the crystal orientation of grain growth. The obtained pattern's surface morphology is layered and deepened as a space structure with a regular pentagon or hexagonal structure;
- The existence of nano-ZrO<sub>2</sub> particles and molybdenum element can refine the grains size and improve the deposition hardness. The deposited Ni-ZrO<sub>2</sub> coating and Ni-Mo-ZrO<sub>2</sub> coating average grain size was small—14.3, 14.2 nm—and the hardness was high—614, 694 HV—respectively;
- Ni-Mo-ZrO<sub>2</sub> composite coating has better tribological and corrosion resistance properties in comprehensive comparison with nickel, Ni-Mo and Ni-ZrO<sub>2</sub> coatings under salt-water conditions. The friction coefficient of Ni-Mo-ZrO<sub>2</sub> is lower under the same conditions. This is directly related to the porous structure and the polarity of nano-ZrO<sub>2</sub> particles of the coating.

**Author Contributions:** Conceptualization, N.L. and H.X.; methodology, N.L. and W.C.; validation, N.L. and W.C.; formal analysis, N.L. and H.X.; investigation, N.L. and H.X.; data curation, L.Z., X.L., and L.L.; writing—original draft preparation, N.L.; writing—review and editing, N.L. All authors have read and agreed to the published version of the manuscript.

**Funding:** The Project was Supported by The Tribology Science Fund of State Key Laboratory of Tribology.

**Acknowledgments:** Thanks are due to testing center of Zhejiang normal university institute of physical chemistry for assistance with the experiments for valuable discussion.

**Conflicts of Interest:** The authors declare no conflict of interest.

## References

1. Wang, R.; Chen, S.; Ma, X.; Liang, J.; Liu, C. Laser direct deposition Mo-Ni-ZrO<sub>2</sub> composited alloy gradient coating. *Acta Mater. Compos. Sin.* **2017**, *34*, 1989–1996.
2. Li, N.; Gao, C. Microstructure and electrochemical properties of the electrodeposited Ni-Mo/ZrO<sub>2</sub> alloy coating. *Mater. Sci. Technol.* **2011**, *19*, 104–109.
3. Laszczyńska, A.; Winiarski, J.; Szczygieł, B.; Szczygieł, I. Electrodeposition and characterization of Ni-Mo-ZrO<sub>2</sub> composite coatings. *Appl. Surf. Sci.* **2016**, *369*, 224–231. [[CrossRef](#)]
4. Kim, Y. Preparation of Ni-ZrO<sub>2</sub> composites via mechanochemistry processes and their catalytic properties. *J. Ceram. Process. Res.* **2016**, *17*, 905–909.
5. Zhang, Y.; Ding, S.; Song, T.; Zhang, Y. Microwave dielectric properties of temperature stable MO-ZrO<sub>2</sub>-Ta<sub>2</sub>O<sub>5</sub> ceramics. *J. Alloys Compd.* **2019**, *798*, 194–203. [[CrossRef](#)]
6. Beltowska-Lehman, E.; Bigos, A.; Indyka, P.; Kot, M. Electrodeposition and characterisation of nanocrystalline Ni-Mo coatings. *Surf. Coat. Technol.* **2012**, *211*, 67–71. [[CrossRef](#)]
7. Wasekar, N.P.; Bathini, L.; Sundararajan, G. Tribological behavior of pulsed electrodeposited Ni-W/SiC nanocomposites. *J. Mater. Eng. Perform.* **2018**, *27*, 5236–5245. [[CrossRef](#)]
8. Huang, B.; Song, C.; Liu, Y.; Gui, Y. Microstructure characterization and wear-resistant properties evaluation of an intermetallic composite in Ni-Mo-Si system. *Materials* **2017**, *10*, 130. [[CrossRef](#)]
9. Wu, C.; Lou, X.; Jia, C. Porous Ni-Mo-Co Hydroxide nanoflakes on carbon cloth for supercapacitor application. *J. Nanosci. Nanotechnol.* **2019**, *19*, 272–276. [[CrossRef](#)]
10. Hu, J.; Shi, Y.N.; Lu, K. Thermal analysis of electrodeposited nano-grained Ni-Mo alloys. *Scr. Mater.* **2018**, *154*, 182–185. [[CrossRef](#)]
11. Gubicza, J.; Pereira, P.H.R.; Kapoor, G.; Huang, Y.; Vadlamani, S.S.; Langdon, T.G. Annealing-induced hardening in ultrafine-grained Ni-Mo alloys. *Adv. Eng. Mater.* **2018**, *20*, 1800184. [[CrossRef](#)]
12. Gui, Y.L.; Song, C.Y.; Yang, L.; Qin, X.L. Microstructure and tribological properties of NiMo/Mo<sub>2</sub>Ni<sub>3</sub>Si intermetallic “in-situ” composites. *J. Alloys Compd.* **2011**, *509*, 4987–4991.
13. Cui, C.; Zhu, X.; Liu, S.; Li, Q.; Zhang, M.; Zhu, G.; Wei, S. Effect of nano-sized ZrO<sub>2</sub> on high temperature performance of Mo-ZrO<sub>2</sub> alloy. *J. Alloys Compd.* **2018**, *768*, 81–87. [[CrossRef](#)]
14. Yun, S.U.; Gulians, V. Surface coverage effects on water gas shift activity of ZrO<sub>2</sub> supported Mo sulfide catalysts. *Catal. Commun.* **2019**, *138*, 105810. [[CrossRef](#)]
15. da Silva, F.C.; Tunes, M.A.; Edmondson, P.D.; Lima, N.B.; Sagás, J.C.; Fontana, L.C.; Schön, C.G. Grid-assisted magnetron sputtering deposition of nitrogen graded TiN thin films. *Appl. Sci.* **2020**, *2*, 865. [[CrossRef](#)]
16. Tunes, M.A.; Vishnyakov, V.M.; Camara, O.; Greaves, G.; Edmondson, P.D.; Zhang, Y.; Donnelly, S.E. A candidate accident tolerant fuel system based on a highly concentrated alloy thin film. *Mater. Today Energy* **2019**, *12*, 356–362. [[CrossRef](#)]
17. Wasekar, N.P.; Verulkar, S.; Vamsi, M.V.N.; Sundararajan, G. Influence of molybdenum on the mechanical properties, electrochemical corrosion and wear behavior of electrodeposited Ni-Mo alloy. *Surf. Coat. Technol.* **2019**, *370*, 298–310. [[CrossRef](#)]
18. Golgovici, F.; Pumnea, A.; Petica, A.; Manea, A.C.; Brincoveanu, O.; Enachescu, M.; Anicai, L. Ni-Mo alloy nanostructures as cathodic materials for hydrogen evolution reaction during seawater electrolysis. *Chem. Pap.* **2018**, *72*, 1889–1903. [[CrossRef](#)]
19. Li, N.; Chen, W.; Lu, L.; Gao, C. Electrodeposition behavior of polycrystalline Ni-Mo-La composite in alkaline solution. *Coatings* **2018**, *8*, 299. [[CrossRef](#)]
20. Wijten, J.H.J.; Riemersma, R.L.; Gauthier, J.; Mandemaker, L.D.B.; Verhoeven, M.W.G.M.; Hofmann, J.P.; Chan, K.; Weckhuysen, B.M. Electrolyte effects on the stability of Ni-Mo cathodes for the hydrogen evolution reaction. *ChemSusChem* **2019**, *12*, 3491–3500. [[CrossRef](#)]
21. Marlot, A.; Kern, P.; Landolt, D. Pulse plating of Ni-Mo alloys from Ni-rich electrolytes. *Electrochim. Acta* **2002**, *48*, 29–36. [[CrossRef](#)]
22. Yagi, S.; Kawakami, A.; Murase, K.; Awakura, Y. Ni-Mo alloying of nickel surface by alternating pulsed electrolysis using molybdenum(VI) baths. *Electrochim. Acta* **2007**, *52*, 6041–6051. [[CrossRef](#)]
23. Wasekar, N.P.; Haridoss, P.; Seshadri, S.K.; Sundararajan, G. Influence of mode of electrodeposition, current density and saccharin on the microstructure and hardness of electrodeposited nanocrystalline nickel coatings. *Surf. Coat. Technol.* **2016**, *291*, 130–140. [[CrossRef](#)]

24. Zhao, W.; Li, W.; Li, X.; Gong, S.; Vitos, L.; Sun, Z. Thermo-mechanical properties of Ni-Mo solid solutions: A first-principles study. *Comput. Mater. Sci.* **2019**, *158*, 140–148. [[CrossRef](#)]
25. Rezaeioloum, A.; Aliofkhaezai, M.; Karimzadeh, A. Electrodeposition of Ni-Mo and Ni-Mo-(nano Al<sub>2</sub>O<sub>3</sub>) multilayer coatings. *Surf. Eng.* **2018**, *34*, 423–432. [[CrossRef](#)]
26. Ahmad, Y.H.; Mohamed, A.M.A.; Golden, T.D.; Souza, N.D. Electrodeposition of nanocrystalline Ni-Mo alloys from alkaline glycinate solutions. *Int. J. Electrochem. Sci.* **2014**, *9*, 6438–6450.
27. Uhlig, H.H.; Bond, P.; Feller, H. Corrosion and passivity of molybdenum-nickel alloys in hydrochloric acid. *J. Electrochem. Soc.* **1963**, *110*, 650–653. [[CrossRef](#)]
28. Huang, P.C.; Hou, K.H.; Sheu, H.H.; Ger, M.D.; Wang, G.L. Wear properties of Ni–Mo coatings produced by pulse electroforming. *Surf. Coat. Technol.* **2014**, *258*, 639–645. [[CrossRef](#)]
29. Vamsi, M.V.N.; Wasekar, N.P.; Sundararajan, G. Sliding wear of as-deposited and heat-treated nanocrystalline nickel-tungsten alloy coatings. *Wear* **2018**, *412*, 136–143. [[CrossRef](#)]



© 2020 by the authors. Licensee MDPI, Basel, Switzerland. This article is an open access article distributed under the terms and conditions of the Creative Commons Attribution (CC BY) license (<http://creativecommons.org/licenses/by/4.0/>).